

Quantifying surfactant adsorption at fluid interfaces by combining X-ray reflection and simulations

Kay-Robert Dormann,^{*,†} Joshua Reed,[†] Daniel Mitlewski,[†] Matej Kanduč,[‡]
Benno Liebchen,[†] and Emanuel Schneck^{*,†}

[†]*Institute for Condensed Matter Physics, Technische Universität Darmstadt, Germany*

[‡]*Jožef Stefan Institute, Ljubljana, Slovenia*

E-mail: kay-robert.dormann@pkm.tu-darmstadt.de; emanuel.schneck@pkm.tu-darmstadt.de

Abstract

Adsorption of surfactants to fluid interfaces occurs in daily-life and technological contexts like dish washing and oil spill remediation. The surfactant surface coverage Γ governs interface characteristics like tension γ , viscoelastic properties, and the stability of thin foam films. Directly measuring Γ as a function of the bulk concentration c is highly desirable but challenging, particularly for non-ionic surfactants that lack easily detectable labels. Here, we propose a generic approach to deduce the adsorption isotherm $\Gamma(c)$: As a first step, we use atomistic molecular dynamics simulations of surfactant-loaded air/water interfaces with known Γ to obtain interfacial electron density profiles. From these profiles, we then compute theoretical X-ray reflectivity curves, which we compare with experimental measurements to find the matching c . We focus on two non-ionic surfactants (C_{12}EO_6 and $\beta\text{-C}_{12}\text{G}_2$) with previously verified force fields to demonstrate how this combined approach of experiments

and simulations can determine the adsorption isotherm. By using the equation of state $\gamma(\Gamma)$ from simulations, our results replicate the measured surface tension isotherms $\gamma(c)$.

Keywords: monolayer, surface tension, critical micelle concentration, adsorption models

Introduction

Surfactants are small amphiphilic molecules that accumulate at air/water and oil/water interfaces. They thereby lower the interfacial tension and are commonly used as cleaning agents and to stabilize foams and emulsions^{1–3}. Because surfactants are technologically so important⁴, with annual production in the billion-dollar/euro range, great efforts are being made for the rational design of surfactants with particular characteristics and functionalities. On the fundamental level, various thermodynamic models have been developed over the past decades^{5–7} to describe the experimentally most accessible quantities, like the interfacial tension γ and the interfacial viscoelastic moduli, both as functions of the surfactant bulk concentration c . In all these models, the surfactant excess Γ at the interface, i.e., the concentration-dependent number of adsorbed surfactants per surface area, is a central parameter. Unfortunately, the *adsorption isotherm* $\Gamma(c)$ is difficult to determine experimentally on a quantitative level. What is typically measured instead is the *surface tension isotherm* $\gamma(c)$. In thermal equilibrium, the two concentration-dependent quantities are coupled through the Gibbs equation,

$$\Gamma(c) = -\frac{1}{k_{\text{B}}T} \frac{\text{d}\gamma(c)}{\text{d}\ln(c)}, \quad (1)$$

where $k_{\text{B}}T$ is the thermal energy. However, as noted earlier^{8–10}, this relation is often of limited practical use and can still involve ambiguities, such that an independent experimental determination of Γ is required.

The most direct way to determine the surfactant excess involves the reflection of neutrons, X-rays, and light¹⁰. Neutron reflectometry (NR) is most sensitive when deuterated

surfactants are used in combination with so-called non-reflecting water^{8,11,12}. Such measurements are relatively fast but can only be performed with deuterated surfactants and with the few horizontal reflectometers at powerful neutron sources, such that they are not suited for routine experiments. Ellipsometry with visible light is fast and simple but relies on the approximation of a homogeneous and isotropic surfactant refractive index and requires independent calibration, e.g., from independent NR measurements^{13,14}. For surfactants with covalently-bound unique elements like phosphorus or sulfur or ionic surfactants with quasi-bound counterions, total-reflection X-ray fluorescence (TRXF)^{15,16} offers an elegant route to determining Γ ^{10,17}. However, this technique is inapplicable to non-ionic surfactants without unique chemical elements, which constitute a substantial fraction of the surfactants nowadays utilized.

X-ray reflectometry (XRR)^{18,19} and the related GIXOS technique^{20,21} are powerful tools to characterize fluid interfaces structurally in terms of their electron density profile. So far, they have however almost exclusively been applied to insoluble surfactants²² or lipids²³. Γ is then typically known *a priori* from surface diffraction in case of crystalline arrangements²⁴ or from well-calibrated pressure/area isotherms. For water-soluble surfactants, which usually do not assume ordered structures and for which pressure/area isotherms cannot be obtained, Γ can only be deduced from the interfacial electron density profiles themselves, which is non-trivial and usually ambiguous because electron density contributions from the surfactants and the displaced water molecules have to be disentangled accurately.

In the present work, we demonstrate that Γ can be extracted reliably from XRR and GIXOS curves when the analysis is aided by molecular dynamics (MD) simulations, which correctly capture surfactant in-plane arrangements, conformations, and hydration. For water-insoluble lipids, such a procedure has already been proven successful^{25,26}. Here, we focus on two technologically important yet chemically very different non-ionic surfactants without any elemental labels, the oligo-ethylene-glycol (OEG) surfactant $C_{12}EO_6$ and the glycosurfactant β - $C_{12}G_2$. We find that XRR and GIXOS in combination with MD simu-

lations give consistent results. Moreover, they reproduce the experimental surface tension isotherm $\gamma(c)$, when integrating the obtained adsorption isotherm with the *equation of state* (EoS), $\gamma(\Gamma)$, which is accessible to MD but not to the experiments.

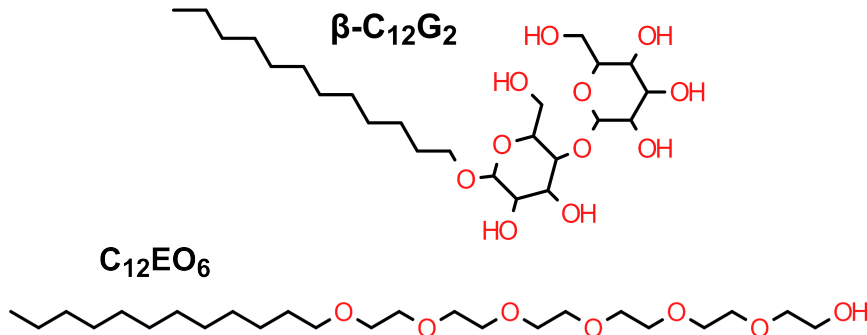


Figure 1: Chemical structures of the surfactants investigated.

Results and discussion

The chemical structures of the two surfactants investigated are shown in Fig. 1. Both comprise a saturated C_{12} alkyl chain and a non-ionic hydrophilic headgroup. The headgroup of hexa(oxyethylene)-lauryl-ether ($C_{12}EO_6$) is a flexible, chain-like linear OEG with six repeat units with only one hydrogen bond (HB) donor per surfactant. In contrast, n-dodecyl- β -D-maltoside (β - $C_{12}G_2$) carries a comparatively rigid disaccharide headgroup with numerous HB donors and acceptors, which were demonstrated to form inter-surfactant HBs^{27,28} that contribute to in-plane cohesion.

$C_{12}EO_6$

Fig. 2 shows X-ray reflectivity curves $R(q_z)$ of the interface between air and aqueous solutions of $C_{12}EO_6$ at systematically increasing bulk concentrations c , ranging from 0.5 to 30 μM , all below the critical micelle concentration ($\text{CMC} \approx 70 \mu\text{M}$, ref. 29). In this regime, the surface coverage Γ increases monotonically with increasing bulk concentration³⁰. Surfactant adsorption typically leads to the formation of distinct layers in the electron density profile

and thus gives rise to reflectivity minima called Kiessig fringes¹⁹, whose q_z -positions depend on the layer thickness. Indeed, the reflectivity curves in Fig. 2 exhibit systematic changes with increasing concentration c , primarily concerning the appearance of a reflectivity minimum that gradually moves toward lower q_z . In other words, the reflectivity curves encode information on the layer thickness and therefore also on Γ . But even though it is possible to extract the approximate electron density profiles from the reflectivity data with slab-based models^{10,28,31}, these alone do not allow reconstructing Γ in a reliable manner because electron density contributions from the surfactants and from the displaced water molecules cannot simply be disentangled.

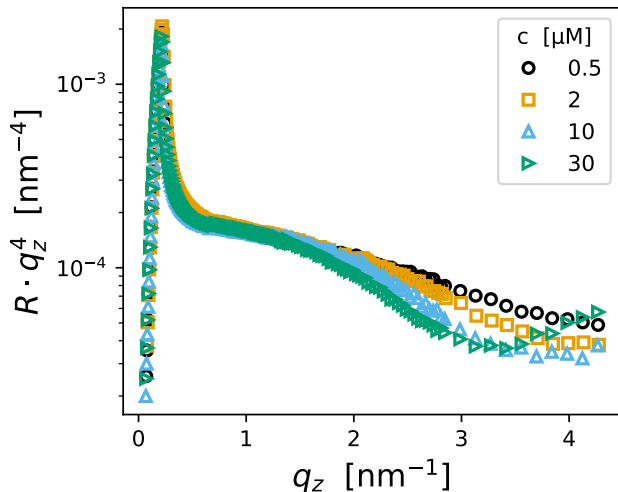


Figure 2: XRR curves $R(q_z)$ of the surfaces of aqueous $C_{12}EO_6$ solutions with bulk concentrations ranging from 0.5 to 30 μM , all below the CMC. For clarity, the curves are plotted as $R \cdot q_z^4$ on a logarithmic scale as a function of q_z .

By contrast, MD simulations readily allow us to impose a desired value of Γ by placing the corresponding number of surfactants at the air/water interface in the simulation box with a fixed area, as has previously been demonstrated for lipids^{25,26}. Γ then stays constant over the simulation time (here: 300 ns, see Methods section) because exchange with the aqueous bulk occurs on much longer time scales³². Fig. 3A shows a snapshot from such a simulation (see the Methods section for technical details). The simulation box contains a water layer of about 3.8 nm thickness whose two interfaces with the vacuum (representing air) are covered

with a certain number of surfactants (here: 48 C_{12}EO_6 molecules per interface, corresponding to $\Gamma = 2.0 \text{ nm}^{-2}$), which are pinned there because of the hydrophobic effect. The molecules are oriented with their hydrophilic headgroups towards the water layer, as imposed by their amphiphilic character³³. Fig. 3B shows the associated electron density profile $\rho_e(z)$ across the simulation box in z direction. The water layer was made to be thick enough so that the center features bulk properties, as evidenced from the featureless electron density plateau in the middle of the profile, with $\rho_e = 333 \text{ e}^-/\text{nm}^3$, in good agreement with the well-known experimental value ($\rho_e = n_e^W \rho_M^W N_A / M_W = 334 \text{ e}^-/\text{nm}^3$, where $n_e^W = 10$ is the number of electrons per water molecule, $M_W = 18 \text{ g mol}^{-1}$ is the molecular mass, $\rho_M^W = 1000 \text{ kg m}^{-3}$ is the mass density of liquid water, and N_A is Avogadro's constant).

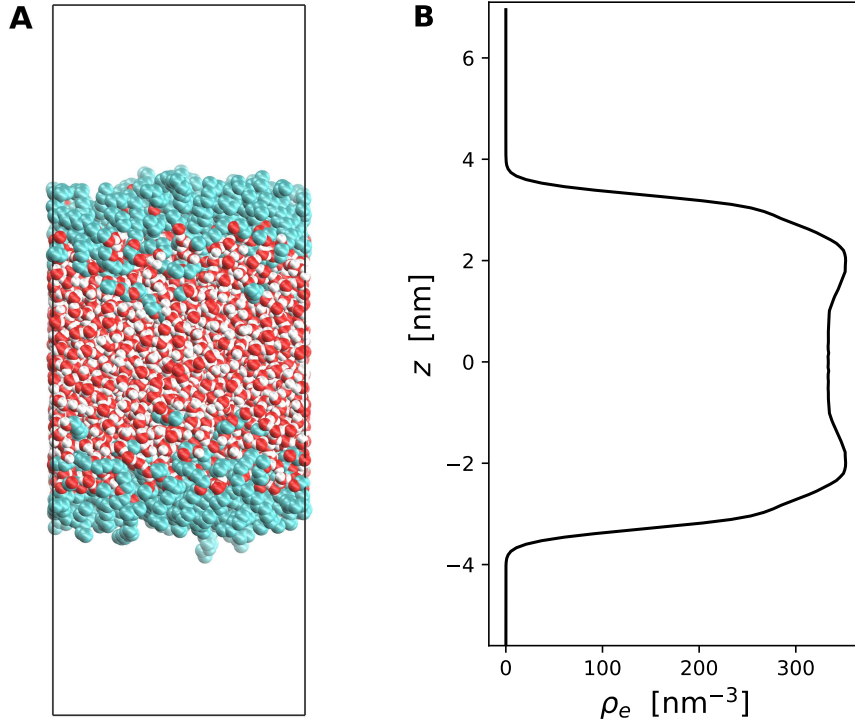


Figure 3: (A) Simulation snapshot of a water layer with 48 C_{12}EO_6 surfactants on each surface, corresponding to $\Gamma = 2.0 \text{ nm}^{-2}$. CH_2 groups and CH_3 groups (both represented as united atoms) are shown in light blue, oxygen atoms in red, and polar hydrogen atoms in white. The periodic simulation box is indicated with a rectangle. (B) Associated electron density profile $\rho_e(z)$ in the direction perpendicular to the interfaces.

Fig. 4A shows the simulation-based one-sided electron density profiles that realistically

represent single, surfactant-loaded interfaces between the two quasi-infinitely extended media, air and water. The profiles are computed from simulations with various choices of Γ , ranging from 0 to 2.9 nm^{-2} , as imposed by the maximal surfactant number of 72 per interface in the simulation box. Higher coverages lead to unrealistically low (or even negative) surface tensions (see Fig. 8A). In the absence of surfactants ($\Gamma = 0$), the profile of the bare water surface exhibits a monotonic transition from $\rho_e = 0$ to the bulk value mentioned before ($\rho_e = 333 \text{ e}^-/\text{nm}^3$). As Γ increases, the profiles change systematically in that they gradually build up a distinct headgroup-related density maximum between the hydrocarbon chain region and the water region. These systematic changes in the electron density profiles rationalize the systematic changes of the reflectivity curves in Fig. 2 because the adsorption isotherm $\Gamma(c)$ increases monotonically, as mentioned before. Fig. 4B shows the theoretical XRR curves calculated from the Γ -dependent one-sided electron density profiles as described in the Methods section. The similarities with the experimental XRR curves in Fig. 2 are striking. Most importantly, the trends when increasing the surface coverage in the theoretical XRR curves are consistent with those when increasing the bulk concentration in the experimental XRR curves.

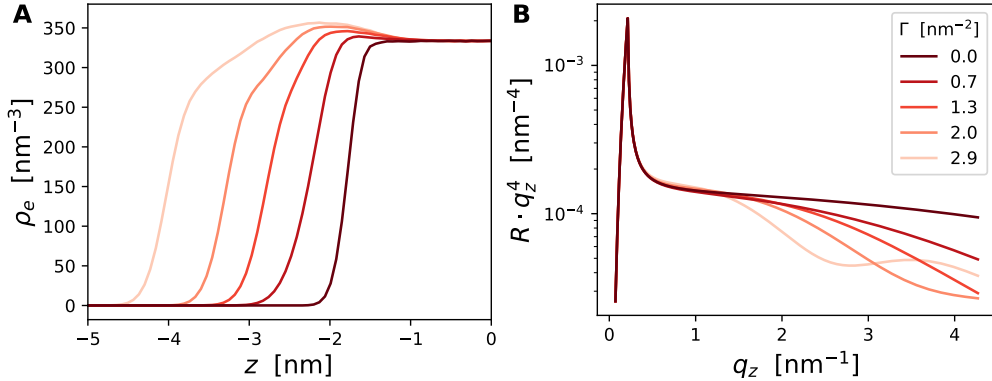


Figure 4: (A) One-sided electron density profiles from simulations with various surface coverages of C_{12}EO_6 surfactants (see legend in panel B). (B) Associated XRR curves. For clarity, the curves are plotted as $R \cdot q_z^4$ on a logarithmic scale as a function of q_z .

In order to determine the surface coverages that match best the experimental XRR curves obtained at various bulk concentrations, we performed a systematic comparison with

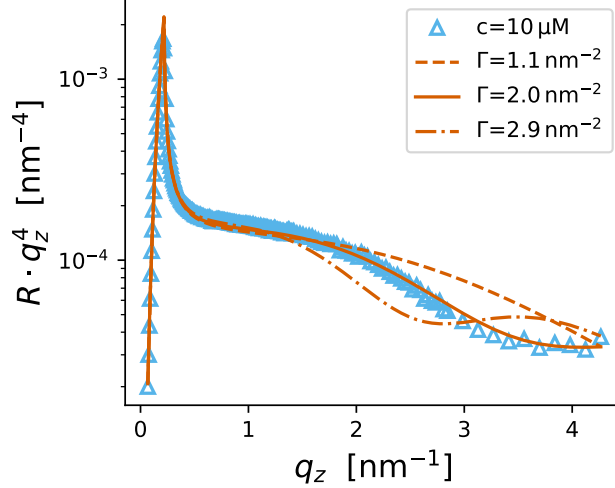


Figure 5: Experimental XRR curve for $C_{12}EO_6$ at $c = 10 \mu\text{M}$ (symbols) together with theoretical XRR curves (lines) corresponding to simulations with three different surface coverages. For clarity, the curves are plotted as $R \cdot q_z^4$ on a logarithmic scale as a function of q_z . Only $\Gamma = 2.0 \text{ nm}^{-2}$ leads to good agreement with the experimental reflectivity data.

the theoretical XRR curves computed for the different Γ values. The fit quality F of each Γ value was the deviation between the experimental and theoretical XRR curves (Eq. 7) after applying to the latter an adjustable flat background not captured by the theoretical curves. Fig. 5 shows the overlay of a representative experimental XRR curve ($C_{12}EO_6$, $c = 10 \mu\text{M}$) with theoretical XRR curves for three different Γ values, of which only one achieves a good fit quality, while the two others fail to reproduce the experimental data.

One aspect to be considered is the potential influence of inconsistent interface roughness in experiments and simulations on the comparison between the respective XRR curves. This is because the apparent amplitude of capillary wave roughness not only depends on the interface tension, but also on the in-plane length scale at which the interface is probed^{34,35}. This length scale may be effectively smaller in the simulation box than in the experiment, depending on the coherence length of the X-ray beam. We therefore consider the effect of elevated roughness in the theoretical reflectivity curves, implemented by convoluting the MD-derived electron density profiles (Eq. 4) with a Gaussian function of width σ (Eq. 3), where σ ranges from 0 to 0.4 nm in 8 steps. The resulting smearing-out of the electron density profile and, in turn, the influence of this procedure on the theoretical XRR curves

are shown in the Supporting Information (Fig. S1).

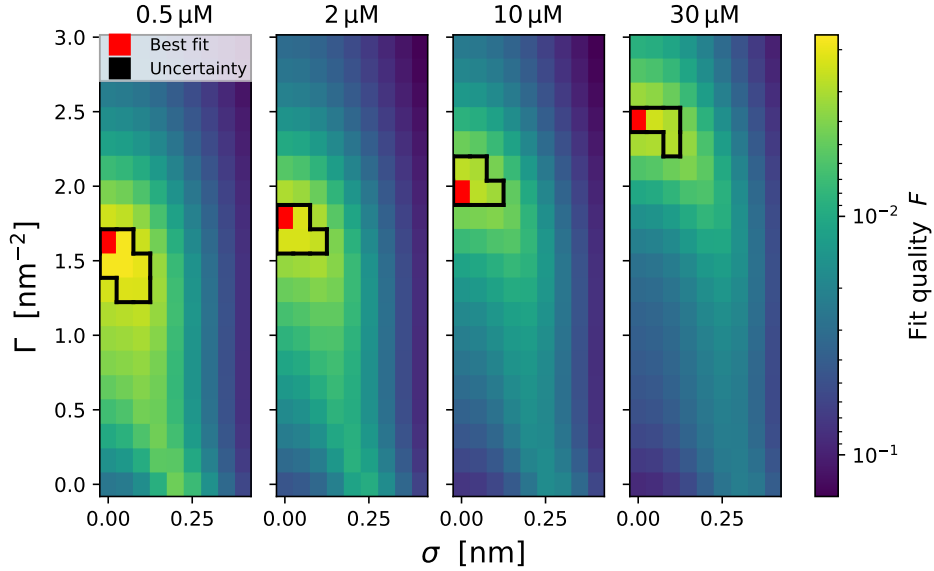


Figure 6: Heat map of the quality of the fits between the experimental XRR curves (Eq. 7) recorded for four $C_{12}EO_6$ bulk concentrations (indicated on the top) and the theoretical XRR curves for varied surface coverage Γ (vertical axis) and roughening parameters σ (horizontal axis). The best-matching parameter combinations are marked in red, while the uncertainty regions are surrounded by black lines.

Fig. 6 shows an overview of the fit quality F (Eq. 7) of the theoretical XRR curves to the experimental XRR curves obtained at all $C_{12}EO_6$ bulk concentrations. For each concentration, F was calculated systematically for all Γ and σ values and presented in the form of a heat map. The best-matching combination of Γ and σ at each concentration is indicated with a red grid point, while the uncertainty region, estimated as described in the Methods section, is surrounded by a black line. It can be seen that, for all bulk concentrations, the fit quality is best for $\sigma = 0$, meaning that the interface roughness in the simulations does not significantly underestimate the effective roughness seen in the XRR experiments (We come back to this point in context with the GIXOS experiments presented later).

The surface coverage that yields the best agreement with the experimental data systematically increases with c . A plot of the adsorption isotherm $\Gamma(c)$ constructed by associating the best-matching surface coverage to each bulk concentration is shown in Fig. 7. The error

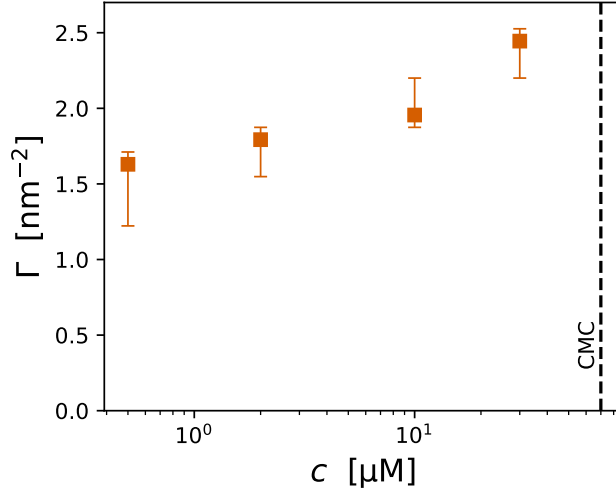


Figure 7: Adsorption isotherm $\Gamma(c)$ of C_{12}EO_6 as constructed from the simulation-assisted analysis of experimental XRR curves. The CMC is indicated with a dashed vertical line. Error bars correspond to the uncertainty regions in Fig. 6.

bars correspond to the uncertainty regions in Fig. 6. Γ is seen to increase monotonically with increasing bulk concentration, approximately linearly with the logarithm of the concentration. For the highest bulk concentration investigated ($c = 30 \mu\text{M} < \text{CMC}$), $\Gamma \approx 2.4 \text{ nm}^{-2}$ is obtained, which coincides with an area per molecule of $A_{\text{mol}} = 1/\Gamma \approx 0.42 \text{ nm}^2$, which is slightly lower than the 0.50 nm^2 estimated earlier²⁹ and about twice the cross-sectional area of around 0.20 nm^2 required per stretched (all-trans) alkyl chain in a chain-crystalline arrangement²⁴. The significantly larger area requirement must be attributed to the fact that adsorption layers of surfactants with C_{12} chains generally do not form such ordered all-trans arrangements and that the area requirement of the OEG headgroup is substantially larger than that of alkyl chains, not least because the loss of conformational entropy required for a stretched-out configuration cannot be compensated by direct hydrogen bonding²⁷. Parameter-based thermodynamic models for the interpretation of tensiometric $\gamma(c)$ curves have predicted maximal coverages Γ in the range of 1.6 to 2.0 nm^{-2} for C_{12}EO_6 ^{36–38}.

Our interim result is that we have established the adsorption isotherm of C_{12}EO_6 . It can be considered very reliable because the primary aspects extracted from the MD simulations for this purpose concerned molecular volumes and conformational flexibility, which are gen-

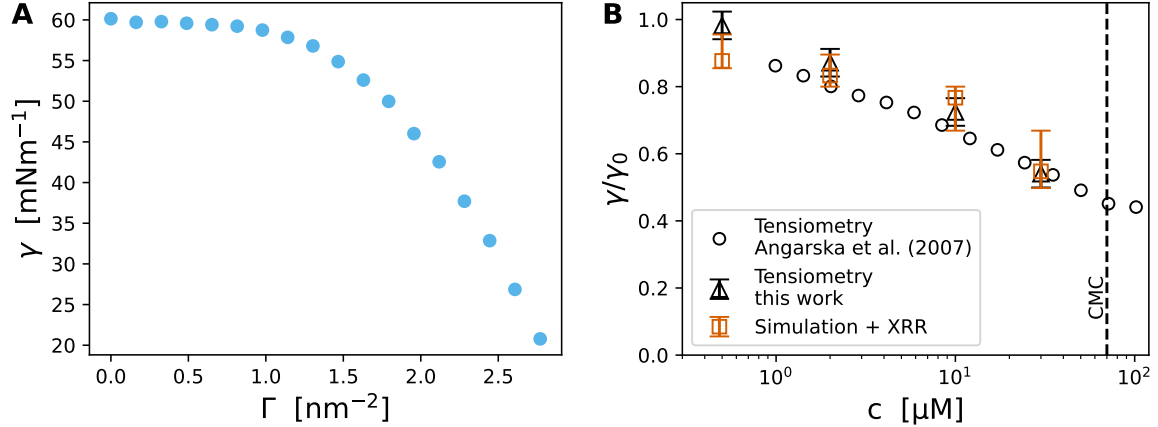


Figure 8: (A) Equation of state $\gamma(\Gamma)$ of $C_{12}EO_6$ as obtained in the simulations. Note that the water model used predicts a bare-water surface tension of $\gamma_0 = 60$ mNm⁻¹. (B) Surface tension isotherm $\gamma(c)$ reconstructed from the equation of state and from the adsorption isotherm $\Gamma(c)$ and comparison with independent tensiometric measurements from the present work and from the literature³⁹.

erally well captured by all force fields, as was pointed out recently for the case of lipids²⁶. In the next step, we turn our attention to the equation of state $\gamma(\Gamma)$, shown in Fig. 8A. It is obtained from the MD simulations through analysis of the pressure tensor³³, as described in the Methods section. The tension γ is seen to decay monotonically with increasing Γ , first slowly and then fast, when steric repulsion becomes dominant⁹. With $\gamma_0 = 60$ mNm⁻¹, the tension of the bare water surface (at $\Gamma = 0$) produced by the employed water model is significantly lower than the experimental value ($\gamma_0 = 72$ mNm⁻¹), an aspect to which we come back later. It should also be noted that the equation of state is more sensitive to the force field than the electron density profiles from which we reconstructed the adsorption isotherm because the former has a subtle dependence on polar and non-polar interaction parameters. We would therefore like to assess how well it reproduces the experimental equation of state. Unfortunately, $\gamma(\Gamma)$ is not directly accessible to experiments. With $\Gamma(c)$ and $\gamma(\Gamma)$ at hand, we can, however, construct, by elimination of Γ , the experimentally well accessible surface tension isotherm $\gamma(c)$, which constitutes an indirect manifestation of the equation of state³². Fig. 8B shows a comparison between the surface tension isotherm constructed here on the basis of XRR measurements and MD simulations with those measured tensiometrically by

ourselves (see Methods section) and by Angarska et al.³⁹. To eliminate the effect of the discrepancy between experiments and simulations with regard to the tension γ_0 of the bare water surface, the comparison is made in terms of the reduced surface tension, γ/γ_0 . We find remarkable agreement between the simulation results and the experimental measurements, which suggests that the employed force field reproduces the equation of state well. Conversely, we are hereby introducing a promising route to the experimental validation of surfactant force fields.

β -C₁₂G₂

For the second surfactant investigated, β -C₁₂G₂ (with CMC = 150 μ M)²⁹, we use the same procedure, but primarily with synchrotron-based GIXOS data, recorded and modeled as described in the Methods section. Application of the procedure also to GIXOS (commonly performed because of its superior time resolution) is suited to assess the general applicability across different X-ray reflection techniques. Complementary XRR measurements are then used for cross-validation (see further below). Fig. 9 shows the fit quality of the concentration-dependent GIXOS data of β -C₁₂G₂ as a function of Γ and σ , again in the form of a heat map. The underlying GIXOS data (Fig. S2) with fits (Fig. S3, S4) are shown in the Supporting Information. As in the case of the XRR data from C₁₂EO₆, we find a monotonic increase of the best-matching surface coverage with increasing bulk concentration. However, for the GIXOS data of β -C₁₂G₂, we obtain the best agreement with the experimental data when the MD-derived electron density profiles are convoluted with a finite roughening parameter, $\sigma \lesssim 0.2$ nm, especially at higher concentrations/coverages (see Fig. 9). Whether this stems from the apparent roughness seen by the technique or with slightly different behavior of β -C₁₂G₂ in experiment and simulation cannot be concluded with certainty. The resulting adsorption isotherm $\Gamma(c)$ is shown in Fig. 10A (open squares). It is seen to increase monotonically with c and exhibits a tendency of saturation at around $\Gamma \approx 2$ nm⁻² as c approaches the CMC, in line with the expectation. The filled circles indicate the results obtained with additional

XRR measurements (see Supporting Information for the corresponding heat maps). The agreement between the GIXOS-based and the XRR-based data is overall reassuring, with the exception of the data points at the lowest concentration ($c = 1 \mu\text{M}$), where we currently have no explanation for the discrepancy.

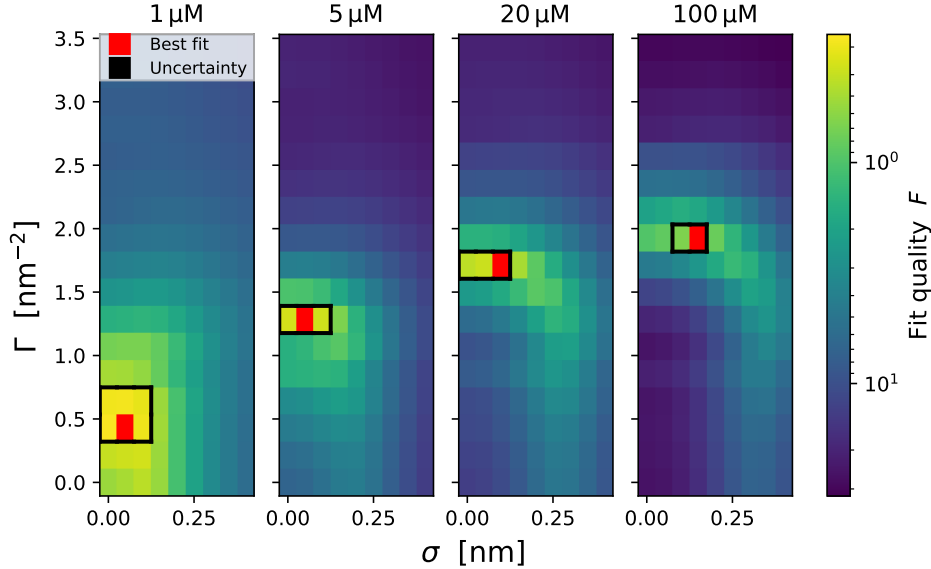


Figure 9: Heat map of the quality of the fits between the experimental GIXOS curves recorded for four $\beta\text{-C}_{12}\text{G}_2$ bulk concentrations (indicated on the top) and the theoretical GIXOS curves for varied surface coverage (vertical axis) and roughening parameters (horizontal axis). The best-matching parameter combination is marked in red, while the uncertainty region is surrounded by a black line.

The simulation-derived equation of state of $\beta\text{-C}_{12}\text{G}_2$ is shown in Fig. 10B for two different simulation box sizes. Unlike the monotonically decaying curve for C_{12}EO_6 , $\beta\text{-C}_{12}\text{G}_2$ features a non-monotonic trend with a maximum of γ at intermediate coverages around $\Gamma \approx 1.5 \text{ nm}^{-2}$. This “hump”, with values exceeding the surface tension of pure water, corresponds to negative surface pressures. Such values indicate metastable states of either a continuous monolayer under lateral tension or a condensed monolayer with a pore. The latter leads to a stronger tension increase for smaller pores (as shown in the Supporting Information), which rationalizes the more pronounced hump for the smaller simulation box. Both metastable scenarios in the simulations correspond to a two-phase-coexistence of gas and condensed phase in the macroscopic limit. This means that, for comparison with exper-

iments, the humps in Fig. 10B would have to be replaced with an almost constant surface tension slightly below γ_0 , followed by a decrease at $\Gamma \approx 2 \text{ nm}^{-2}$ once the surface becomes fully covered by a condensed monolayer. The fact that this hump is observed for $\beta\text{-C}_{12}\text{G}_2$ but not for C_{12}EO_6 points to substantially stronger cohesion between $\beta\text{-C}_{12}\text{G}_2$ surfactants, most likely mediated by hydrogen bonding between their disaccharide headgroups^{27,28}. Whether this cohesion is strong enough to drive a genuine gas/condensed transition in reality remains unclear. Such a transition implies a discontinuous increase in the surface coverage, $\Gamma(c)$, at the coexistence bulk concentration and, according to Eq. 1, a corresponding kink in the surface tension isotherm $\gamma(c)$, as observed for some other surfactants⁴⁰ but not as decisively for $\beta\text{-C}_{12}\text{G}_2$ ²⁹.

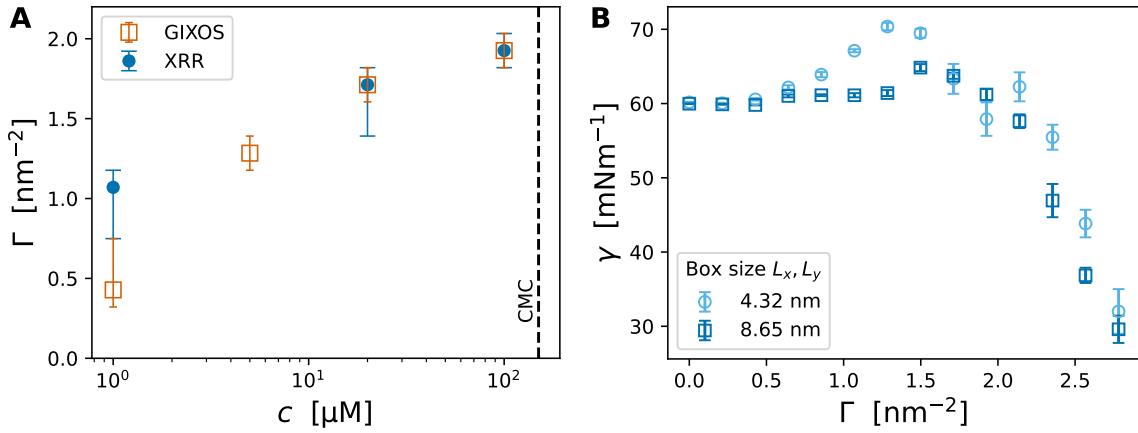


Figure 10: (A) Adsorption isotherm $\Gamma(c)$ of $\beta\text{-C}_{12}\text{G}_2$ as constructed from the simulation-assisted analysis of experimental GIXOS and XRR curves. The CMC is indicated with a dashed vertical line. Error bars correspond to the uncertainty regions in Fig. 9 (GIXOS) and in Fig. S5 (XRR). (B) Equation of state $\gamma(\Gamma)$ of $\beta\text{-C}_{12}\text{G}_2$ as obtained in simulations with different box sizes.

Conclusions

To quantify the concentration-dependent adsorption of surfactants to air/water interfaces, we combined XRR, measured with a conventional laboratory X-ray source, with molecular dynamics simulations, which serve for accurate and robust data interpretation. With our

approach, we were able to determine $\Gamma(c)$ accurately for two common surfactants, C_{12}EO_6 and $\beta\text{-C}_{12}\text{G}_2$. Our results reproduce the experimental surface tension isotherm $\gamma(c)$ of C_{12}EO_6 , which constitutes a validation of the force field employed for this surfactant. For $\beta\text{-C}_{12}\text{G}_2$, we found consistency when analyzing XRR data and synchrotron-based GIXOS data. Knowledge of the surfactant coverage is valuable for all surfactant-related research^{9,10}. Our approach enables an accurate quantification of the surfactant coverage, which can be performed routinely with conventional laboratory instruments and does not require the use of synchrotrons or neutron sources. The adsorption isotherms obtained in this way can provide a valuable basis for the interpretation of tensiometric data with parameter-based thermodynamics models and for the validation and refinement of force fields for molecular dynamics simulations.

Materials and methods

Chemicals and sample preparation

C_{12}EO_6 and $\beta\text{-C}_{12}\text{G}_2$ were purchased from Merck (Darmstadt, Germany) and from Glycon (Luckenwalde, Germany), respectively, and used as received. H_2O was ultrapure Milli-Q water (specific resistivity: $18\text{ M}\Omega\text{ cm}$) from a purification system (Elga, Purelab classic). Aqueous solutions of the surfactants at the desired concentrations were prepared by adding the respective surfactant amounts to H_2O in glass bottles previously cleaned by extensive rinsing with ethanol and H_2O . The solutions were then stirred and let rest for at least 30 min before pouring them into the troughs used for XRR or GIXOS measurements.

Surface tension measurements

The surface tension was measured in a Teflon trough by Riegler & Kirstein (Potsdam, Germany) with a Wilhelmy paper plate. Because no *in situ* calibration measurement with pure water is possible, the uncertainty in γ was estimated as $\pm 2\text{ mN m}^{-1}$.

XRR

XRR measurements were performed at room temperature, (20 ± 1) °C, using a D8 Advance reflectometer (Bruker AXS, Karlsruhe, Germany) with horizontal sample geometry and a vertical goniometer, allowing the liquid surface to be studied without being disturbed during the measurements. A Teflon trough (Riegler & Kirstein GmbH, Potsdam, Germany), with the dimensions of 11.5 cm parallel and 32.5 cm perpendicular to the beam propagation, was enclosed in a box with Kapton windows through which the incident and reflected X-ray beams pass. XRR curves were measured in the $\theta - 2\theta$ geometry, where θ is the incident angle. A conventional X-ray tube with a copper anode (Cu K_α , wavelength $\lambda = 0.154$ nm) was used to generate an X-ray beam with a line focus. The beam was monochromatized with a Göbel mirror (W/Si multilayer) and collimated through two narrow horizontal slits of 0.1 mm width with a switchable Cu attenuator in between. Soller slits ($\Delta\theta_x = 25$ mrad) were placed after the last horizontal slit and directly in front of the detector. The intensity was recorded with a Våntec-1 line detector (Bruker AXS, Germany). Intensities were corrected using the known attenuation factors and corrected for the variable footprint where necessary. Finally, the angular XRR curves were transformed to XRR curves as a function of the perpendicular scattering vector component, $q_z = 4\pi \sin(\theta/\lambda)$.

GIXOS

GIXOS measurements were carried out at the beamline P08 at storage ring PETRA III of Deutsches Elektronen-Synchrotron (DESY, Hamburg, Germany) as described in reference³¹, from which the following text is partially reproduced. The Langmuir trough (Riegler & Kirstein, Potsdam, Germany) was located in a hermetically sealed container with Kapton windows, and the temperature was kept at 20 °C by a thermostat. The container was constantly flushed with a stream of humidified helium (He) to prevent air scattering and the generation of reactive oxygen species. The synchrotron X-ray beam was monochromatized to a photon energy of 15 keV, corresponding to a wavelength of $\lambda = 0.0827$ nm. The incident an-

gle was adjusted to $\theta_i = 0.07^\circ$, slightly below the critical angle of total reflection, $\theta_c = 0.082^\circ$. A ground glass plate was placed approximately 0.3 to 1 mm beneath the illuminated area of the monolayer in order to reduce mechanically excited surface waves. Analogous to conventional X-ray reflectometry, GIXOS allows reconstructing the interfacial electron density profile (i.e., the laterally-averaged structure of the molecular layers in the direction perpendicular to the surface) from the q_z -dependent scattering intensity, however, at fixed incident angle. The details of this technique are described elsewhere^{20,21,41}. The q_z -dependence of the diffuse scattering intensity $I(q_{xy} \neq 0, q_z)$ recorded at low-enough yet non-zero q_{xy} with a linear detector (Pilatus 100k, Dectris AG, Switzerland, with settings described elsewhere²⁸). $I(q_{xy} \neq 0, Q_z)$ contains information equivalent to that of the conventional reflectivity $R(q_z)$ and can be transformed as:

$$I(q_{xy} \neq 0, q_z) \propto R(q_z) \frac{V(q_z)}{R_F(q_z)} \quad (2)$$

to a good approximation, where $R_F(q_z)$ is the reflectivity of an ideal interface between the two bulk media and $V(q_z)$ is the Vineyard function⁴². In the present work, the GIXOS signal was measured 0.3° off the plane of incidence horizontally, corresponding to $q_{xy} = 0.4 \text{ nm}^{-1}$ at $q_z = 0$.

Molecular dynamics simulations

Parts of the following section are replicated from previous publications^{28,32}. For C_{12}EO_6 , we used the GROMOS-compatible 2016H66 force field^{43,44} and for $\beta\text{-C}_{12}\text{G}_2$, we used the GROMOS 53a6 force field^{45–47}. Both surfactant force fields adopt a united-atom treatment of the aliphatic groups. Water was described with the SPC/E model⁴⁸. The simulation setup consisted of a 3 to 4 nm thick water slab replicated in the x and y directions via periodic boundary conditions, placed in a simulation box of dimensions around $4.3 \times 4.3 \times 12 \text{ nm}$ for $\beta\text{-C}_{12}\text{G}_2$ and around $5 \times 5 \times 14 \text{ nm}$ for C_{12}EO_6 . The water slab was loaded with the same

number of surfactants on its two surfaces. Variable surfactant coverages were achieved by symmetrically varying the number of surfactants on both surfaces while leaving the box dimensions fixed. The simulation topology and run files are available in the supporting information⁴⁹. The simulations were performed with the GROMACS simulation package^{50,51}, version 2021.5. Electrostatics was treated using the particle-mesh-Ewald method^{52,53} with a 1.4 nm real-space cutoff. The Lennard-Jones interactions were cut off at 1.4 nm. The simulations were performed with an integration time step of 2 fs in the constant-volume (NVT) ensemble. Temperature was maintained at 293.15 K using the velocity-rescale thermostat⁵⁴ with a time constant of 0.1 ps. Each simulation was 300 ns long. However, following initial investigations of common measures of equilibration, the first 100 ns were discarded from the analysis. The surface tension was calculated from the diagonal elements p_{xx} , p_{yy} , and p_{zz} of the pressure tensor, as $\gamma = L_z[2p_{zz} - (p_{xx} + p_{yy})]/(2N_{\text{int}})$, where L_z is the simulation box size in z direction and $N_{\text{int}} = 2$ is the number of interfaces in the simulation box³³.

Electron density profiles from the MD simulations

Electron density profiles $\rho_e(z)$ were obtained from molecular dynamics simulations with the "gmx density" tool of GROMACS⁵¹. For this procedure, center-of-mass subtraction and symmetrization were used to enable averaging over multiple time-steps and to improve statistics, respectively. The z -axis was divided into slabs of equal thickness (0.07 nm for C_{12}EO_6 and 0.06 nm for $\beta\text{-C}_{12}\text{G}_2$).

The roughening parameter σ (see Results section) was applied to the electron density profiles through convolution with a Gaussian function of the form

$$g(z) = \frac{1}{\sigma\sqrt{2\pi}} e^{-\frac{1}{2}\frac{z^2}{\sigma^2}}, \quad (3)$$

such that the roughened (smeared-out) electron density profile $\rho_e^\sigma(z)$ is given as

$$\rho_e^\sigma(z) = \int_{-\infty}^{\infty} \rho_e(z') g(z - z') dz'. \quad (4)$$

Calculation of theoretical XRR curves

With the discretized set of electron density slabs at hand, the partial waves reflected at each slab/slab interface were computed according to the Fresnel equations and summed in a phase-correct manner using the Parratt recursion formalism⁵⁵ to determine the reflected intensity under idealized conditions, $R_{\text{ideal}}(q_z)$. For comparison with the experimental XRR curves, three possible corrections were implemented, namely a scale factor s for the absolute intensity, a constant intensity background I_{bg} , and an offset Δq_z , which absorbs minor angular misalignments that affect the precise apparent position of the critical angle of total reflection. The resulting theoretical XRR curves then have the form

$$R(q_z) = s R_{\text{ideal}}(q_z - \Delta q_z) + I_{\text{bg}}. \quad (5)$$

Calculation of theoretical GIXOS curves

The starting point for the GIXOS curve calculation is the ideal XRR curve $R_{\text{ideal}}(q_z)$. According to Eq. 2, the GIXOS intensity was then calculated as

$$I_{\text{GIXOS}}(q_z) = s \frac{V(q_z - \Delta q_z) R_{\text{ideal}}(q_z - \Delta q_z)}{R_{\text{F}}(q_z - \Delta q_z)} + I_{\text{bg}} \quad (6)$$

with the parameters s , I_{bg} , Δq_z introduced before.

Fitting procedure and fit quality assessment

Irrespective of the technique (XRR or GIXOS), the starting point is the combination of an experimental curve and a theoretical curve $R_{\text{ideal}}(q_z)$, where the latter depends on the choice

of Γ and σ in the simulation. To optimize the match between the two curves, the parameters s , I_{bg} , and Δq_z in Eqs. 5 and 6 have to be adjusted. The best-matching values of s and Δq_z are characteristic of each experimental curve and independent of Γ or σ . They are therefore constrained prior to the actual fit. The only remaining free parameter for each choice of Γ and σ is then I_{bg} , which is optimized in a classical least-square minimization procedure. For XRR, the fit quality function minimized was

$$F = \frac{1}{N} \sum_{i=1}^N [\log(R_i^{\text{th}} q_{z,i}^4) - \log(R_i^{\text{ex}} q_{z,i}^4)]^2, \quad (7)$$

where R^{th} and R^{ex} are the theoretical and experimental reflectivities, respectively, and N is the number of data points (i.e., the number of q_z values at which the reflectivity was measured). For GIXOS, the fit quality function minimized was

$$F = \frac{1}{N} \sum_{i=1}^N (I_{\text{GIXOS},i}^{\text{th}} - I_{\text{GIXOS},i}^{\text{ex}})^2, \quad (8)$$

where $I_{\text{GIXOS}}^{\text{th}}$ and $I_{\text{GIXOS}}^{\text{ex}}$ are the theoretical and experimental GIXOS intensities, respectively. For GIXOS, the fitting range was limited to the consensus range of validity ($q_z > 3 \cdot q_z^c$, where q_z^c is the q_z -value at the critical angle of total reflection).

The uncertainty margin for the parameters Γ and σ was defined as the point at which the deviation F increases by a factor of 1.3 with respect to the optimal parameter set. This experience-based definition is somewhat arbitrary but, in our opinion, reflects the true uncertainty much better than estimates based solely on the statistical errors⁵⁶, which are much smaller but neglect systematic uncertainties, as pointed out earlier⁵⁷.

Supporting information

Influence of the roughening parameter σ ; GIXOS data on $\beta\text{-C}_{12}\text{G}_2$; Fit quality heat maps for $\beta\text{-C}_{12}\text{G}_2$; Influence of the system size on the surface tension in a simulation containing a

condensed monolayer with a pore.

Conflicts of interest

There are no conflicts of interest to declare.

CRedit author statement

Conceptualization: MK, BL, ES; Formal Analysis: KD; Investigation: KD, JR, DM; Methodology: KD, MK, ES; Project administration: ES, BL; Resources: BL, ES; Supervision: ES, BL; Validation: KD, JR, MK, ES; Visualization: KD; Writing – original draft: KD, JR, ES; Writing – review & editing: KD, JR, MK, BL, ES.

Acknowledgement

We acknowledge DESY (Hamburg, Germany), a member of the Helmholtz Association HGF, for the provision of experimental facilities. Parts of this research were carried out at PETRA III, and we would like to thank Chen Shen and Rene Kirchhof for assistance in using P08 and Milena Lippmann for assistance in the chemistry lab. Beamtime was allocated for proposal I-11015005. M.K. acknowledges financial support from the Slovenian Research and Innovation Agency ARIS (contracts P1-0055 and J1-4382). We thank Olaf Soltwedel for support with XRR experiments and Reinhard Miller for insightful comments.

References

- (1) Stubenrauch, C.; Miller, R. Stability of foam films and surface rheology: an oscillating bubble study at low frequencies. *The Journal of Physical Chemistry B* **2004**, *108*, 6412–6421.

- (2) Georgieva, D.; Cagna, A.; Langevin, D. Link between surface elasticity and foam stability. *Soft Matter* **2009**, *5*, 2063–2071.
- (3) Langevin, D. Recent Advances on Emulsion and Foam Stability. *Langmuir* **2023**, *39*, 3821–3828.
- (4) Myers, D. *Surfactant science and technology*; John Wiley & Sons, 2020.
- (5) Frumkin, A. Electrocapillary curve of higher aliphatic acids and the state equation of the surface layer. *Z. Phys. Chem* **1925**, *116*, 466–470.
- (6) Liggieri, L.; Ferrari, M.; Massa, A.; Ravera, F. Molecular reorientation in the adsorption of some CiEj at the water-air interface. *Colloids and Surfaces A: Physicochemical and Engineering Aspects* **1999**, *156*, 455–463.
- (7) Fainerman, V. B.; Aksenenko, E. V.; Makievski, A. V.; Nikolenko, M. V.; Javadi, A.; Schneck, E.; Miller, R. Particular behavior of surface tension at the interface between aqueous solution of surfactant and alkane. *Langmuir* **2019**, *35*, 15214–15220.
- (8) Li, Z.; Dong, C.; Thomas, R. Neutron reflectivity studies of the surface excess of gemini surfactants at the air- water interface. *Langmuir* **1999**, *15*, 4392–4396.
- (9) Kovalchuk, V.; Aksenenko, E.; Schneck, E.; Miller, R. Surfactant Adsorption Layers: Experiments and Modeling. *Langmuir* **2023**, *39*, 3537–3545.
- (10) Schneck, E.; Reed, J.; Seki, T.; Nagata, Y.; Kanduč, M. Experimental and simulation-based characterization of surfactant adsorption layers at fluid interfaces. *Advances in Colloid and Interface Science* **2024**, 103237.
- (11) Staples, E.; Thompson, L.; Tucker, I.; Penfold, J.; Thomas, R.; Lu, J. Surface composition of mixed surfactant monolayers at concentrations well in excess of the critical micelle concentration. A neutron scattering study. *Langmuir* **1993**, *9*, 1651–1656.

- (12) Lu, J.; Hromadova, M.; Simister, E.; Thomas, R.; Penfold, J. Neutron reflection from hexadecyltrimethylammonium bromide adsorbed at the air/liquid interface: the variation of the hydrocarbon chain distribution with surface concentration. *The Journal of Physical Chemistry* **1994**, *98*, 11519–11526.
- (13) Manning-Benson, S.; Parker, S. R.; Bain, C. D.; Penfold, J. Measurement of the dynamic surface excess in an overflowing cylinder by neutron reflection. *Langmuir* **1998**, *14*, 990–996.
- (14) Valkovska, D.; Wilkinson, K. M.; Campbell, R. A.; Bain, C. D.; Wat, R.; Eastoe, J. Measurement of the dynamic surface excess of the nonionic surfactant C8E4OMe by neutron reflection and ellipsometry. *Langmuir* **2003**, *19*, 5960–5962.
- (15) Bloch, J.; Sansone, M.; Rondelez, F.; Peiffer, D.; Pincus, P.; Kim, M.-W.; Eisenberger, P. Concentration profile of a dissolved polymer near the air-liquid interface: X-ray fluorescence study. *Physical review letters* **1985**, *54*, 1039.
- (16) Yun, W.; Bloch, J. X-ray near total external fluorescence method: Experiment and analysis. *Journal of applied physics* **1990**, *68*, 1421–1428.
- (17) Daillant, J.; Bosio, L.; Benattar, J.; Blot, C. Interaction of cations with a fatty acid monolayer. A grazing incidence x-ray fluorescence and reflectivity study. *Langmuir* **1991**, *7*, 611–614.
- (18) Als-Nielsen, J.; McMorrow, D. Elements of Modern X-ray Physics: Second Edition. *Elements of Modern X-ray Physics: Second Edition* **2011**,
- (19) Daillant, J.; Gibaud, A. *X-ray and neutron reflectivity: principles and applications*; Springer, 2008; Vol. 770.
- (20) Mora, S.; Daillant, J.; Luzet, D.; Struth, B. X-ray surface scattering investigation of

- Langmuir films: Phase transitions and elastic properties. *EPL (Europhysics Letters)* **2004**, *66*, 694.
- (21) Wiegart, L.; Struth, B.; Tolan, M.; Terech, P. Thermodynamic and structural properties of phospholipid Langmuir monolayers on hydrosol surfaces. *Langmuir* **2005**, *21*, 7349–7357.
- (22) Als-Nielsen, J.; Kjær, K. *Phase Transitions in Soft Condensed Matter*; Springer, 1989; pp 113–138.
- (23) Kuhl, T.; Majewski, J.; Howes, P.; Kjaer, K.; Von Nahmen, A.; Lee, K.; Ocko, B.; Israelachvili, J.; Smith, G. Packing Stress Relaxation in Polymer- Lipid Monolayers at the Air- Water Interface: An X-ray Grazing-Incidence Diffraction and Reflectivity Study. *Journal of the American Chemical Society* **1999**, *121*, 7682–7688.
- (24) Hermelink, A.; Brezesinski, G. Do unsaturated phosphoinositides mix with ordered phosphatidylcholine model membranes? *Journal of lipid research* **2008**, *49*, 1918–1925.
- (25) Grava, M.; Ibrahim, M.; Sudarsan, A.; Pusterla, J.; Philipp, J.; Rädler, J. O.; Schwierz, N.; Schneck, E. Combining molecular dynamics simulations and x-ray scattering techniques for the accurate treatment of protonation degree and packing of ionizable lipids in monolayers. *The Journal of Chemical Physics* **2023**, *159*.
- (26) Suárez-Lestón, F.; Miettinen, M. S.; Nesterenko, A. Consistent Pressure–Area Isotherms via X-ray Reflectometry and Molecular Simulation. *Colloids and Surfaces A: Physicochemical and Engineering Aspects* **2025**, *726*, 137789.
- (27) Stubenrauch, C.; Hamann, M.; Preisig, N.; Chauhan, V.; Bordes, R. On how hydrogen bonds affect foam stability. *Advances in colloid and interface science* **2017**, *247*, 435–443.

- (28) Kanduč, M.; Schneck, E.; Stubenrauch, C. Intersurfactant H-bonds between head groups of n-dodecyl- β -D-maltoside at the air-water interface. *Journal of colloid and interface science* **2021**, *586*, 588–595.
- (29) Patil, S. R.; Buchavzov, N.; Carey, E.; Stubenrauch, C. Binary mixtures of β -dodecylmaltoside (β -C 12 G 2) with cationic and non-ionic surfactants: micelle and surface compositions. *Soft Matter* **2008**, *4*, 840–848.
- (30) Rosen, M. J.; Kunjappu, J. T. *Surfactants and interfacial phenomena*; John Wiley & Sons, 2012.
- (31) Reed, J.; Grava, M.; Shen, C.; Brezesinski, G.; Schneck, E. Grazing-incidence X-ray diffraction elucidates structural correlations in fluid monolayers of lipids and surfactants. *Nanoscale* **2025**, *17*, 3257–3269.
- (32) Kanduč, M.; Stubenrauch, C.; Miller, R.; Schneck, E. Interface Adsorption versus Bulk Micellization of Surfactants: Insights from Molecular Simulations. *Journal of Chemical Theory and Computation* **2023**,
- (33) Müller, P.; Bonthuis, D. J.; Miller, R.; Schneck, E. Ionic Surfactants at Air/Water and Oil/Water Interfaces: A Comparison Based on Molecular Dynamics Simulations. *Journal of Physical Chemistry B* **2021**, *125*, 406–415.
- (34) Braslau, A.; Deutsch, M.; Pershan, P. S.; Weiss, A. H.; Als-Nielsen, J.; Bohr, J. Surface Roughness of Water Measured by X-Ray Reflectivity. *Physical Review Letters* **1985**, *54*, 114.
- (35) Mitrinovic, D. M.; Zhang, Z.; Williams, S. M.; Huang, Z.; Schlossman, M. L. X-ray reflectivity study of the water- hexane interface. *The Journal of Physical Chemistry B* **1999**, *103*, 1779–1782.

- (36) Eastoe, J.; Dalton, J. S.; Rogueda, P. G.; Crooks, E. R.; Pitt, A. R.; Simister, E. A. Dynamic Surface Tensions of Nonionic Surfactant Solutions. *Journal of Colloid and Interface Science* **1997**, *188*, 423–430.
- (37) Zhmud, B. V.; Tiberg, F.; Kizling, J. Dynamic surface tension in concentrated solutions of CnEm surfactants: a comparison between the theory and experiment. *Langmuir* **2000**, *16*, 2557–2565.
- (38) Yada, S.; Suzuki, T.; Hashimoto, S.; Yoshimura, T. Adsorption and Aggregation Properties of Homogeneous Polyoxypropylene-Polyoxyethylene Alkyl Ether Type Nonionic Surfactants. *Langmuir* **2017**, *33*, 3794–3801.
- (39) Angarska, J.; Stubenrauch, C.; Manev, E. Drainage of foam films stabilized with mixtures of non-ionic surfactants. *Colloids and Surfaces A: Physicochemical and Engineering Aspects* **2007**, *309*, 189–197.
- (40) Aratono, M.; Uryu, S.; Hayami, Y.; Motomura, K.; Matuura, R. Phase transition in the adsorbed films at water/air interface. *Journal of colloid and interface science* **1984**, *98*, 33–38.
- (41) Shen, C.; Zhang, H.; Ocko, B. M. Reconstructing the reflectivity of liquid surfaces from grazing incidence X-ray off-specular scattering data. *Applied Crystallography* **2024**, *57*, 714–727.
- (42) Vineyard, G. H. Grazing-incidence diffraction and the distorted-wave approximation for the study of surfaces. *Physical Review B* **1982**, *26*, 4146.
- (43) Horta, B. A.; Merz, P. T.; Fuchs, P. F.; Dolenc, J.; Riniker, S.; Hünenberger, P. H. A GROMOS-Compatible Force Field for Small Organic Molecules in the Condensed Phase: The 2016H66 Parameter Set. *Journal of Chemical Theory and Computation* **2016**, *12*, 3825–3850.

- (44) Senac, C.; Urbach, W.; Kurtisovski, E.; Hünenberger, P. H.; Horta, B. A.; Taulier, N.; Fuchs, P. F. Simulating Bilayers of Nonionic Surfactants with the GROMOS-Compatible 2016H66 Force Field. *Langmuir* **2017**, *33*, 10225–10238.
- (45) López, C. A.; Sovova, Z.; Van Eerden, F. J.; De Vries, A. H.; Marrink, S. J. Martini force field parameters for glycolipids. *Journal of Chemical Theory and Computation* **2013**, *9*, 1694–1708.
- (46) Van Eerden, F. J.; De Jong, D. H.; De Vries, A. H.; Wassenaar, T. A.; Marrink, S. J. Characterization of thylakoid lipid membranes from cyanobacteria and higher plants by molecular dynamics simulations. *Biochimica et Biophysica Acta (BBA) - Biomembranes* **2015**, *1848*, 1319–1330.
- (47) Oostenbrink, C.; Villa, A.; Mark, A. E.; Van Gunsteren, W. F. A biomolecular force field based on the free enthalpy of hydration and solvation: The GROMOS force-field parameter sets 53A5 and 53A6. *Journal of Computational Chemistry* **2004**, *25*, 1656–1676.
- (48) Berendsen, H. J.; Grigera, J. R.; Straatsma, T. P. The missing term in effective pair potentials. *Journal of Physical Chemistry* **1987**, *91*, 6269–6271.
- (49) Supporting Information: GROMACS simulation files. <https://doi.org/10.48328/tudatalib-2024>.
- (50) Van Der Spoel, D.; Lindahl, E.; Hess, B.; Groenhof, G.; Mark, A. E.; Berendsen, H. J. GROMACS: Fast, flexible, and free. *Journal of Computational Chemistry* **2005**, *26*, 1701–1718.
- (51) Abraham, M. J.; Murtola, T.; Schulz, R.; Páll, S.; Smith, J. C.; Hess, B.; Lindahl, E. GROMACS: High performance molecular simulations through multi-level parallelism from laptops to supercomputers. *SoftwareX* **2015**, *1-2*, 19–25.

- (52) Darden, T.; York, D.; Pedersen, L. Particle mesh Ewald: An $N \cdot \log(N)$ method for Ewald sums in large systems. *The Journal of Chemical Physics* **1993**, *98*, 10089–10092.
- (53) Essmann, U.; Perera, L.; Berkowitz, M. L.; Darden, T.; Lee, H.; Pedersen, L. G. A smooth particle mesh Ewald method. *The Journal of Chemical Physics* **1995**, *103*, 8577–8593.
- (54) Bussi, G.; Donadio, D.; Parrinello, M. Canonical sampling through velocity rescaling. *Journal of Chemical Physics* **2007**, *126*, 14101.
- (55) Parratt, L. G. Surface Studies of Solids by Total Reflection of X-Rays. *Physical Review* **1954**, *95*, 359.
- (56) Bevington, P. R.; Robinson, D. K.; Blair, J. M.; Mallinckrodt, A. J.; McKay, S. Data reduction and error analysis for the physical sciences. *Computers in Physics* **1993**, *7*, 415–416.
- (57) Rodriguez-Loureiro, I.; Scoppola, E.; Bertinetti, L.; Barbetta, A.; Fragneto, G.; Schneck, E. Neutron reflectometry yields distance-dependent structures of nanometric polymer brushes interacting across water. *Soft Matter* **2017**, *13*, 5767–5777.

Quantifying surfactant adsorption at fluid interfaces by combining X-ray reflection and simulations

– Supporting Information –

Kay-Robert Dormann,^{*,†} Joshua Reed,[†] Daniel Mitlewski,[†] Matej Kanduč,[‡]
Benno Liebchen,[†] and Emanuel Schneck^{*,†}

[†]*Institute for Condensed Matter Physics, Technische Universität Darmstadt, Germany*

[‡]*Jožef Stefan Institute, Ljubljana, Slovenia*

E-mail: kay-robert.dormann@pkm.tu-darmstadt.de; emanuel.schneck@pkm.tu-darmstadt.de

Influence of the roughening parameter σ

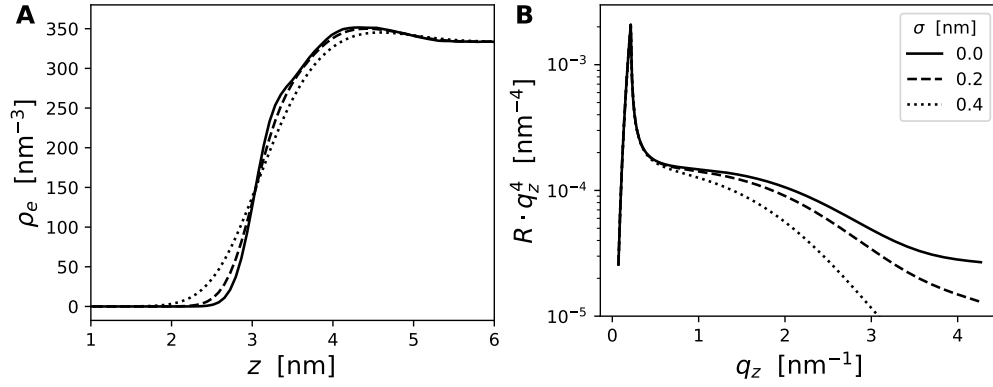


Figure S1: (A) Influence of the roughening parameter σ on the electron density. Original electron density (solid line), $\sigma = 0.2 \text{ nm}$ (dashed), and $\sigma = 0.4 \text{ nm}$ (dotted). (B) Influence on the reflectivity curve (B), where zero background intensity is assumed.

GIXOS data on β -C₁₂G₂

Figure S2 shows GIXOS data obtained with solutions of β -C₁₂G₂ at the concentrations indicated in the figure legend. The electron density profiles obtained in simulations for $0 \leq \Gamma \leq 3.4 \text{ nm}^{-2}$ are shown in Figure S3A. The associated theoretical GIXOS curves are shown in Figure S3B. An example of experimental GIXOS data with theoretical GIXOS curves corresponding to different surface coverages is shown in Figure S4.

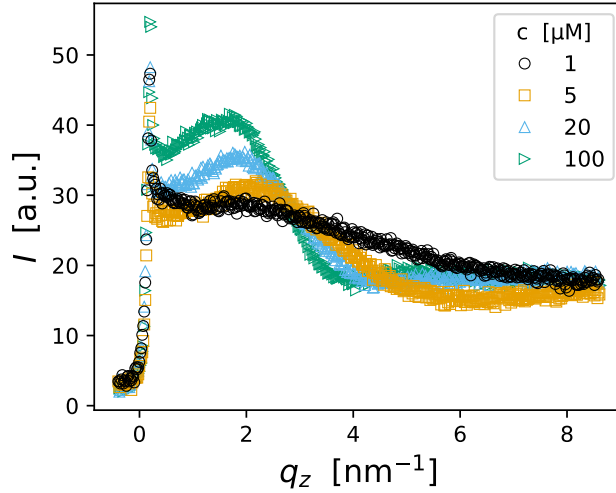


Figure S2: GIXOS measurements on β -C₁₂G₂ at different bulk concentrations c .

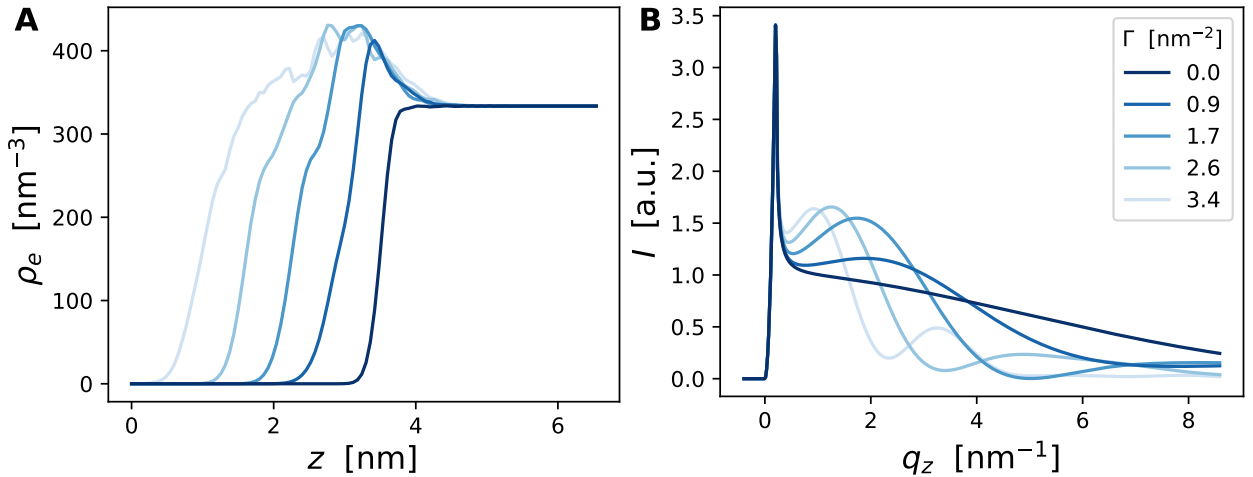


Figure S3: (A) Electron density profiles from MD simulations of β -C₁₂G₂ at different surface coverages (see legend in panel B). (B) Corresponding theoretical GIXOS curves.

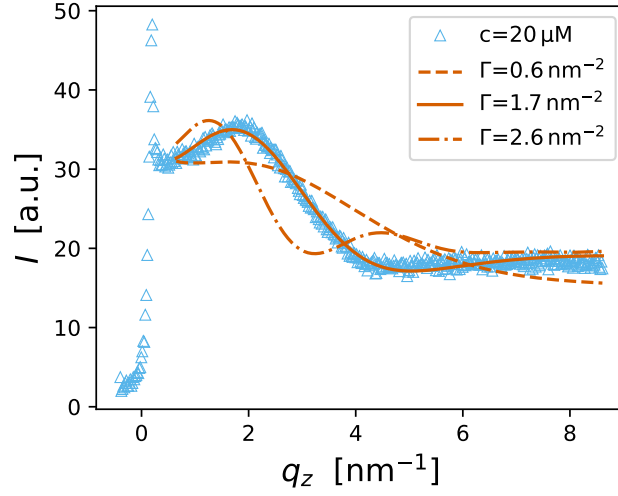


Figure S4: Experimental GIXOS curve for $\beta\text{-C}_{12}\text{G}_2$ at $c = 20 \mu\text{M}$ (symbols) together with theoretical GIXOS curves (lines) corresponding to simulations with three different surface coverages (see legend). Only $\Gamma = 1.7 \text{ nm}^{-2}$ leads to good agreement with the experimental data.

XRR fit quality heat maps for $\beta\text{-C}_{12}\text{G}_2$

The fit quality heat maps for XRR on $\beta\text{-C}_{12}\text{G}_2$ at three bulk concentrations are shown in Figure S5.

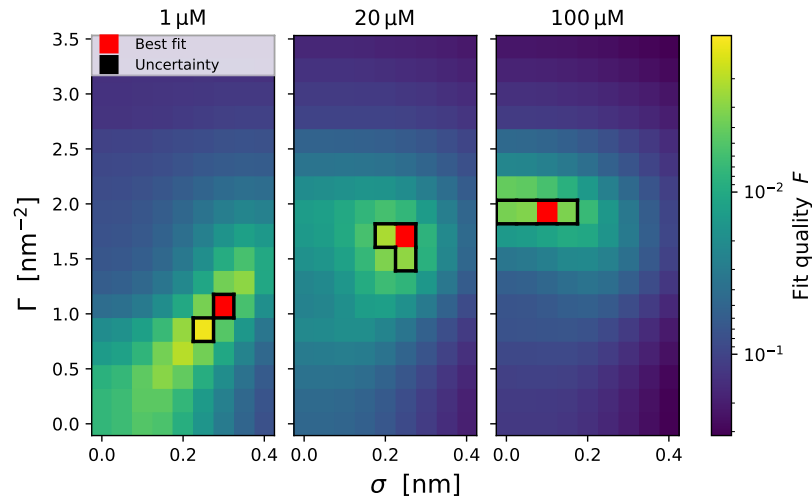


Figure S5: Heat maps of the quality of the fits between the experimental XRR curves recorded for three $\beta\text{-C}_{12}\text{G}_2$ bulk concentrations (indicated on the top) and the theoretical GIXOS curves for varied surface coverage (vertical axis) and roughening parameters (horizontal axis). The best-matching parameter combination is marked in red, while the uncertainty region is surrounded by a black line.

Influence of the system size on the surface tension in a simulation containing a condensed monolayer with a pore

For a condensed surfactant monolayer with a circular pore, the surface tension increment $\Delta\gamma$ generated through the pore's line tension τ is inversely proportional to the pore radius R , as follows from the identity

$$\Delta\gamma = \frac{dG}{dA} = \frac{dG}{dR} \cdot \frac{dR}{dA} = \frac{dG/dR}{dA/dR} = \frac{2\pi\tau}{2\pi R} = \frac{\tau}{R}, \quad (\text{S1})$$

where $L = 2\pi R$ and $A = \pi R^2$ are the circumference and the area of the pore, respectively, and $G = \tau L$ is the excess free energy of the line. For two systems of different sizes but the same surface coverage Γ , the larger system will have a larger pore. Thus, the pore-related tension increment $\Delta\gamma$ will be smaller in the larger system.